공학석사학위논문

전두부 곡률 형상이 항력에 미치는 영향

Effect of the Forebody Curvature on the Drag of an Axi-symmetric Body

2012 년 8 월

서울대학교 대학원

기계항공공학부

장 윤 식

전두부 곡률 형상이 항력에 미치는 영향

Effect of the Forebody Curvature
on the Drag of an Axi-symmetric Body

지도교수 최 해 천

이 논문을 공학석사 학위논문으로 제출함

2012 년 8 월

서울대학교 대학원
기계항공공학부
장 윤 식

장윤식의 공학석사 학위논문을 인준함

2012 년 8 월

위 원 장 : ____________________

부위원장 : ____________________

위　　원 : ____________________

Effect of the Forebody Curvature on the Drag of an Axi-symmetric Body

Yunsik Jang
School of Mechanical and Aerospace Engineering
Seoul National University

Abstract

In the present study, we investigate the effect of forebody curvature on a drag of an axi-symmetric body by numerical simulation. Curvature is applied on ellipsoid with 4:1 aspect ratio and results are compared with 4:1 ellipsoid. The Reynolds number considered are 10^3 and 10^4 based on the free-stream velocity (u_∞) and minor axis of body (d).

At $Re = 10^4$, 4.5% of drag reduction is achieved compared to that of 4:1 ellipsoid. However, at $Re = 10^3$, variation of total drag is little. At both Reynolds number, as curvature increases, pressure drag increases because low pressure occurs around forebody curvature. Contrary to pressure drag, friction drag decreases as curvature increases due to the formation of recirculation bubble on the concave region of curvature. Therefore, reduction of total drag is determined by amount of pressure drag increase and friction drag decrease.

Keywords: Forebody, Curvature, Drag, Ellipsoid

Student number: 2010-24071

Contents

List of Figures

List of Tables

Nomenclature

Roman Symbols

C_D	drag coefficient
C_p	pressure coefficient, $C_p = (p - p_\infty)/\frac{1}{2}\rho u_\infty^2$
d	diameter of a body
N_x, N_r, N_ϕ	number of grid points (streamwise, radial and azimuthal directions, respectively)
p	pressure
q	mass source/sink
Re	Reynolds number, $Re = u_\infty d/\nu$
t	time
u_∞	free-stream velocity
u_x, u_r, u_θ	streamwise, radial and azimuthal velocity components, respectively
x, r, θ	cylindrical coordinate (streamwise, radial and azimuthal directions, respectively)
x, y, z	Cartesian coordinate (y and z correspond to $\theta = 0°$ and $\theta = 90°$, respectively)

Greek Symbols

ϕ_s	separation angle

Superscripts

$\overline{(\,)}$	mean quantity

Subscripts

$(\,)_\infty$	free-stream

Abbreviations

CD	second-order central difference scheme
LES	large eddy simulation
RK3	third-order Runge-Kutta method
QUICK	quadratic upwind interpolation for convective kinematics

Chapter 1

Introduction

Flow control for reducing drag of a bluff body is a challenge in many engineering problems. Various approaches have been conducted to reduce drag of a bluff body. Geometric modification is one of these approaches. Recently, many attempts to reduce the drag on vehicles have been suggested via bio-mimetic engineering. For example, bionic concept car that mimics the shape of boxfish and Shinkansen bullet train from kingfisher, both experience reduced drag over their non-biomimetic counterparts.

In nature, Emperor penguin shows excellent hydrodynamic properties. Their bodies are best described by their multiply-curved outlines (forebody curvature), not observed in other swimming animals. Clark and Bemis (1979) measured drag coefficient of gliding Emperor penguin and suggested that low drag can be attributed to their unique body shape. Bannasch (1998) also performed experimental studies on both live penguins and real-size models of their trunk in a water tank revealing an extremely low drag coefficient. He concluded that viscous drag was reduced by characteristic stepwise pressure and velocity distribution developed along the multiply-curved outlines of body. However, he focused on flow characteristics around penguin, not the effect of forebody curvature. Therefore, the objective of present study is to investigate the effect of forebody curvature on the flow around an axi-symmetric body and to examine the possibility of drag reduction.

The present thesis is organized as follows. Numerical details and model of forebody curvature used in this study are explained in Chapter 2. Results for laminar flow over a forebody at $Re = 10^3$ and turbulent flow at $Re = 10^4$ are presented in Chapter 3. Finally, summary and conclusion are given in Chapter 4.

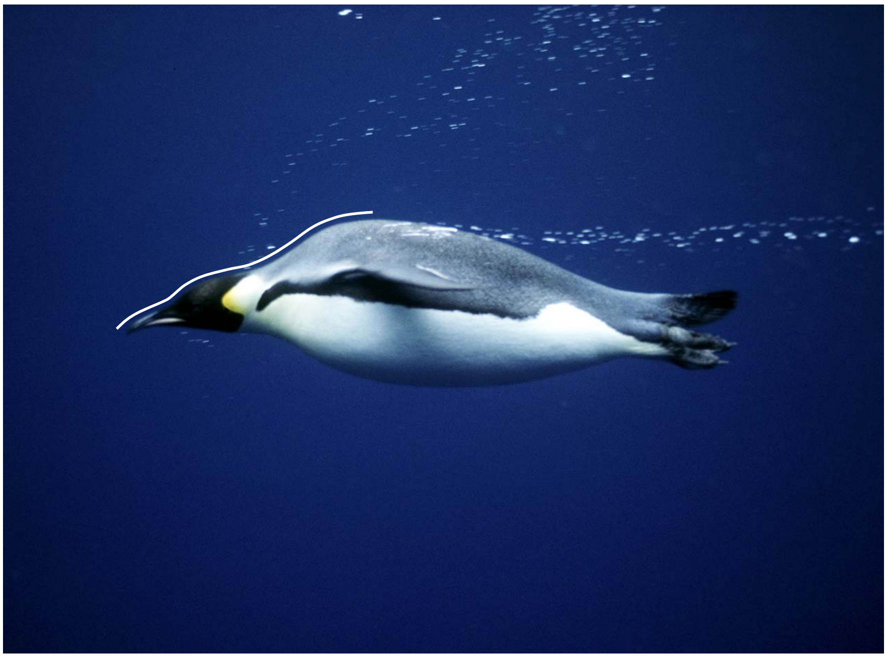

Figure 1.1. Forebody curvature of Emperor penguin.

Chapter 2

Numerical Details

2.1 Governing equations

The governing equations of unsteady incompressible viscous flow are continuity and Navier-stokes equations:

$$\frac{\partial u_i}{\partial t} + \frac{\partial u_i u_j}{\partial x_j} = -\frac{\partial p}{\partial x_i} + \frac{1}{Re}\frac{\partial^2 u_i}{\partial x_j \partial x_j} + f_i, \tag{2.1}$$

$$\frac{\partial u_i}{\partial x_i} - q = 0, \tag{2.2}$$

where x_i's are the cylindrical coordinates, u_i's are the corresponding velocity components, p is the pressure, f_i and q, respectively, are the momentum forcing and the mass source/sink defined on the immersed boundary or inside the body (Kim *et al.* (2001)).

The governing equations of unsteady incompressible viscous flow for large eddy simulation are the filtered continuity and Navier-stokes equations:

$$\frac{\partial \bar{u}_i}{\partial t} + \frac{\partial \bar{u}_i \bar{u}_j}{\partial x_j} = -\frac{\partial \bar{p}}{\partial x_i} + \frac{1}{Re}\frac{\partial^2 \bar{u}_i}{\partial x_j \partial x_j} + \frac{\partial \tau_{ij}}{\partial x_j} + \bar{f}_i, \tag{2.3}$$

$$\frac{\partial \bar{u}_i}{\partial x_i} - \bar{q} = 0, \tag{2.4}$$

where $(\bar{\bullet})$ indicates the filtering operation. Dynamic global model proposed by

Park *et al.* (2006) and Lee *et al.* (2010) are used for obtaining the sub-grid scale stress tensor $\tau_{ij} = \overline{u_i u_j} - \bar{u}_i \bar{u}_j$. All the variables are non-dimensionalized by the minor axis of body d, and the free-stream velocity u_∞. The Reynolds number is defined as $Re = u_\infty d/\nu$, where ν is the kinematic viscosity.

A staggered grid system is employed in this study, and thus u_i and f_i are defined at the cell face, whereas p and q are defined at the cell center. The time-integration method used to solve governing equations is based on a fractional-step method. Hence a pseudo-pressure is used to correct the velocity field and then the continuity equation is satisfied at each computational time step.

In this study, numerical simulations are performed for laminar flows at $Re = 10^3$ and turbulent flows at $Re = 10^4$. Large eddy simulation is conducted for turbulent flows at $Re = 10^4$. We use a second-order semi-implicit time advancement scheme as in Akselvoll & Moin (1996). Consequently, third-order Runge-Kutta method (RK3) is used for the terms treated explicitly and a second-order Crank-Nicolson method is used for the terms treated implicitly. The second-order central difference scheme is used for the spatial derivative terms at $Re = 10^3$. On the other hand, hybrid scheme is used for spatial derivative terms at $Re = 10^4$: third-order QUICK scheme used at laminar accelerating region ($x/d \leq 1$) and second-order central difference elsewhere (Yun *et al.* (2006)).

2.2 Computational domain and boundary conditions

Figure 2.1 shows the coordinate system, domain size and boundary conditions. As explained before, we use the cylindrical coordinate system, where x, r and θ, respectively, denote the streamwise, radial and azimuthal directions. A Cartesian coordinate system (x, y, z) is also used in order to define the drag and lift forces. The computational domain used is $-15 \leq x/d \leq 15$, $0 \leq r/d \leq 15$, and $0 \leq \theta \leq 2\pi$, where ($x/d = 0$, $r/d = 0$) corresponds to the center location of the body. Non-uniform meshes are used with dense resolution in the vicinity of body ($-2 \leq x/d \leq 2$, $0 \leq r/d \simeq 0.5$) for accurate capturing the boundary layer around the body. Consequently, the number of grid points used is $489(x) \times 161(r) \times 2(\theta)$ at $Re = 10^3$ and $673(x) \times 233(r) \times 40(\theta)$ at $Re = 10^4$. A Dirichlet boundary condition ($u_x = u_\infty$, $u_r = 0$, $u_\theta = 0$) is used at the inflow and far-field boundaries ($r/d = 15$), and a convective boundary condition ($\partial u_i/\partial t + c\partial u_i/\partial x = 0$) is used for the outflow boundary, where c is the space-averaged streamwise velocity at the exit.

2.3 Forebody curvature shape

To investigate the effect of forebody curvature, curvature is applied at forebody of 4:1 ellipsoid ($-2 \leq x/d \leq -1$). Three points ($x/d = -1.75$, -1.5, -1.25 for $p1$, $p2$, $p3$, respectively) are used as design parameters. Figure 2.2 shows the placement of the three control points on the forebody of 4:1 ellipsoid. Location of three control points varies in y direction and curvature between the control points is defined by cubicspline interpolation. To investigate the effect of forebody curvature on drag coefficient, the volume of body with forebody curvature is maintained as same as that of 4:1 ellipsoid. Figure 2.3 shows the shape of curvatures. Forebody curvature shapes, Case1, Case2 and Case3, are obtained by varying y position of $p2$ by 0.02, 0.04 and 0.06, respectively, and that of $p1$ and $p3$ is changed to maintain the constant volume. As shown in Figure 2.3, curvature increases as variation of y position of $p2$ increases (from Case1 to Case3).

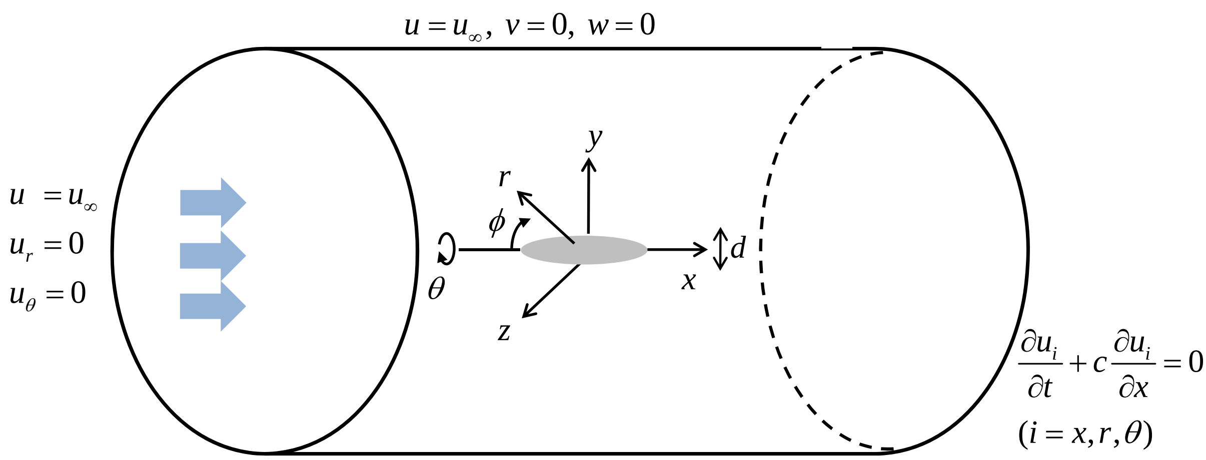

Figure 2.1. Schematic diagram of the coordinates, computational domain and boundary conditions.

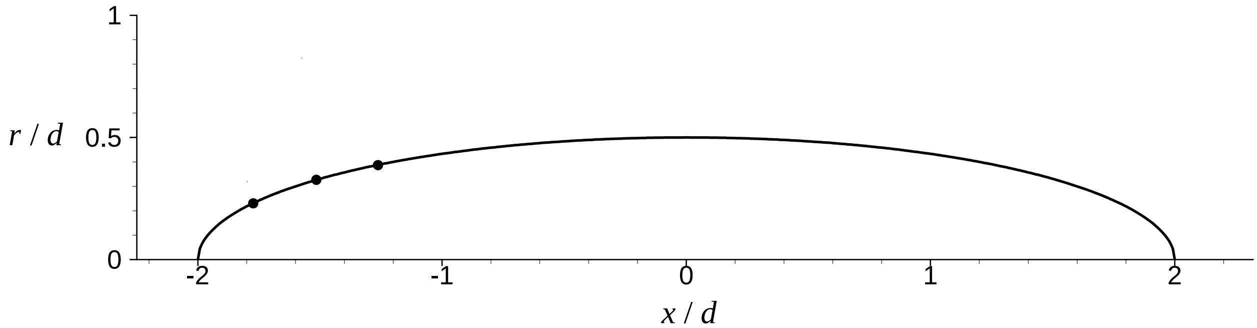

Figure 2.2. Placement of three control points.

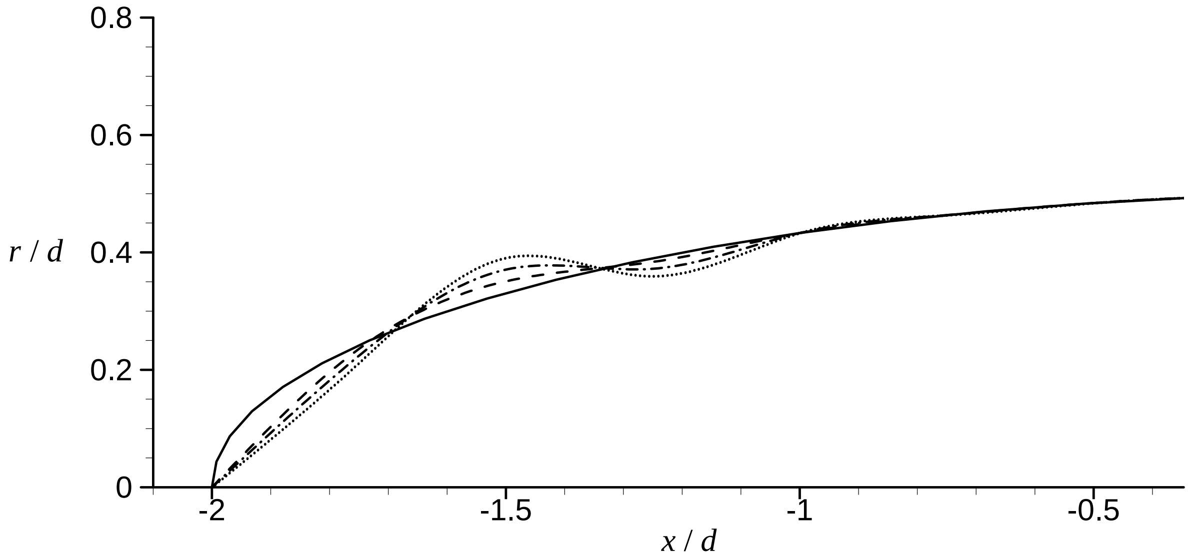

Figure 2.3. Forebody curvature shape. —, 4:1 ellipsoid; - - -, Case1; – · –, Case2; · · · Case3

Chapter 3

Numerical Results

3.1 Effect of forebody curvature at $Re = 10^3$

To investigate the effect of forebody curvature in laminar flow, two-dimensional simulation of laminar flow is performed at $Re = 10^3$. The simulation results, time-averaged drag coefficient ($\overline{C}_d$), time-averaged pressure drag coefficient ($\overline{C}_{dp}$), time-averaged friction drag coefficient ($\overline{C}_{df}$) and separation angle ($\overline{\phi}_s$), are summarized in table 3.1. The separation angle $\overline{\phi}_s$ is measured from a stagnation point and averaged in the azimuthal direction and time.

Separation angle ($\overline{\phi}_s$) shows little difference depending on shape of forebody curvature, indicating that forebody curvature does not affect on flow separation. Figure 3.1 shows the contours of instantaneous spanwise vorticity at $Re = 10^3$. Steady axi-symmetric flow is represented and there is no discernible difference

	$\overline{C}_d$	$\overline{C}_{dp}$	$\overline{C}_{df}$	$\overline{\phi}_s$
Ellipsoid	0.364	0.0636	0.3	171°
Case1	0.364	0.0727	0.291	171°
Case2	0.362	0.0912	0.271	171°
Case3	0.365	0.122	0.243	171°

Table 3.1. Parameters of flow over forebody curvature body at $Re = 10^3$.

in spanwise vorticity contour for all simulation cases.

Figure 3.2 shows streamlines around the forebody curvature for all studied curvatures at $Re = 10^3$. Separation does not occur on the forebody for 4:1 ellipsoid (figure 3.2 (a)) and Case1 (figure 3.2 (b)). However, local separation occurs at $x/d = -1.5$ and recirculation bubble is formed as curvature increases from Case1 to Case2 (figure 3.2 (c)). Due to the recirculation bubble and the reverse flow generated by it, skin friction is negative on the concave region of curvature, and this contributes to the reduction of friction drag. Larger recirculation bubble is observed as curvature increases from Case2 to Case3 (figure 3.2 (d)), indicating lower skin friction for broader region in Case3 compared to Case2.

Time-averaged pressure coefficient (C_p) and time-averaged friction coefficient (C_f) are shown in figure 3.3. As shown in figure 3.3 (a), favorable and adverse pressure gradient occurs along forebody and pressure coefficient shows little difference after $x/d = 0$ for all forebody curvature shapes. As curvature increase from 4:1 ellipsoid to Case1, Case2 and Case3, width of low pressure region around forebody and magnitude of the lowest pressure drag coefficient are increased. Therefore, pressure drag increases as curvature increases because formation of low pressure region on the frontal part of the body indicates larger pressure drag. On the other hand, friction coefficient of the body with forebody curvature at $-1.5 < x/d < -1$ is lower compared to that of 4:1 ellipsoid (figure 3.3 (b)). The position for the lowest friction coefficient is located near $x/d = -1.25$, the lowest point of concave region. Also, width of low friction drag region and magnitude of the lowest friction drag coefficient increase as curvature increases from Case1 to Case2 and Case3, indicating lower friction drag, as expected previously.

In table 3.1, we can check pressure drag increases but friction drag decrease as curvature increases from Case1 to Case2 and Case3 as previously mentioned. Interestingly, total drag does not change even though both pressure and friction drag changed depending on forebody curvature. It is because magnitude of increment of pressure drag and decrement of friction drag are equivalent for all cases at $Re = 10^3$ as shown in table 3.1.

3.2 Effect of forebody curvature at $Re = 10^4$

In the present section, we investigate the effect of forebody curvature in turbulent flow at $Re = 10^4$. The simulation results are presented in table 3.2. Separation angle shows little difference depending on forebody curvature, which is similar trend with laminar flow. Figure 3.4 shows the contours of instantaneous azimutal vorticity at $Re = 10^4$. Separation occurs at similar location and vortex shedding occurs in the wake.

Figure 3.5 shows streamlines around the forebody curvature for all the studied curvatures at $Re = 10^4$. The pattern of streamline is quite similar to that observed in laminar flow over forebody curvature. Local separation does not occur around forebody for 4:1 ellipsoid and Case1, but it occurs for Case2 and Case3. However, size of recirculation bubble is larger compare to that in laminar flow case. In Case3, especially, recirculation bubble is formed over the concave region (Figure 3.5 (d)), whereas it exists inside the concave region at $Re = 10^3$. This affects on shear layer passing over concave region. Also, location for the core of a recirculation bubble moves streamwise direction as curvature increases from Case2 to Case3. This is closely related to skin friction distribution, which is explained in figure 3.6 (b).

Figure 3.6 provides time-averaged pressure coefficient and time-averaged friction coefficient at $Re = 10^4$. The lowest pressure coefficient occurs at

	$\overline{C}_d$	$\overline{C}_{dp}$	$\overline{C}_{df}$	$\overline{\phi}_s$
Ellipsoid	0.121	0.0409	0.0798	161°
Case1	0.121	0.0467	0.0746	161°
Case2	0.116	0.0570	0.0585	161°
Case3	0.124	0.0748	0.0487	162°

Table 3.2. Parameters of flow over forebody curvature body at $Re = 10^4$.

$x/d = -1.5$ and magnitude of it becomes larger as curvature increases, which is similar to laminar flow (figure 3.6 (a)). However, in Case2 and Case3, pressure coefficient does not recover gradually after lowest pressure point. Instead, pressure coefficient remains almost constant in concave region, and recovers around convex region. This means that strength of recirculation bubble is stronger compared to laminar flow. Friction coefficient at $Re = 10^4$ also shows similar trend with that of laminar case (figure 3.6 (b)). As curvature increases, region of low skin friction is enlarged. Similar with pressure coefficient, friction coefficient remains almost constant in concave region. A remarkable trend is that location for the lowest friction coefficient moves streamwise direction as curvature increases. This is closely related to the movement of core of recirculation bubble because reduction of friction drag occurs due to the generated reverse flow by recirculation bubble.

In table 3.2, we can see the relation of curvature with pressure drag and friction drag. Similar to laminar flow, pressure drag increases as curvature increases, whereas friction drag decreases as curvature increases. However, total drag changes depending on forebody curvature contrary to laminar flow. As curvature increases from 4:1 ellipsoid to Case1 and Case2, total drag decreases gradually because decrement of friction drag is larger than increment of pressure drag. However, when curvature increases more from Case2 to Case3, amount of pressure drag increase is larger than that of friction drag reduction which results in total drag increase. Therefore, it can be concluded that drag decreases as curvature increases to certain amount, but it increases when curvature is too large. Maximum drag reduction is achieved in Case2, about 4.5%

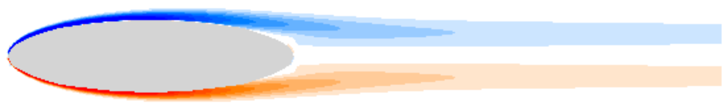

(a)

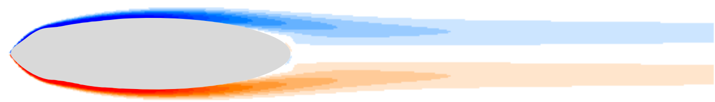

(b)

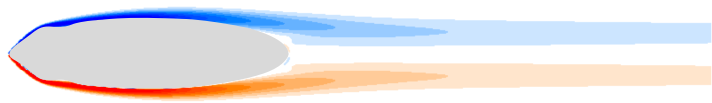

(c)

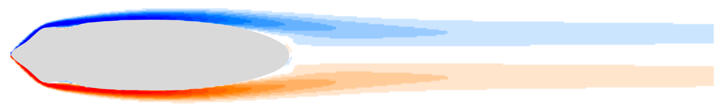

(d)

Figure 3.1. Contours of the instantaneous spanwise vorticity in x-y plane at $Re = 10^3$: (a) 4:1 ellipsoid; (b) Case1; (c) Case2; (d) Case3.

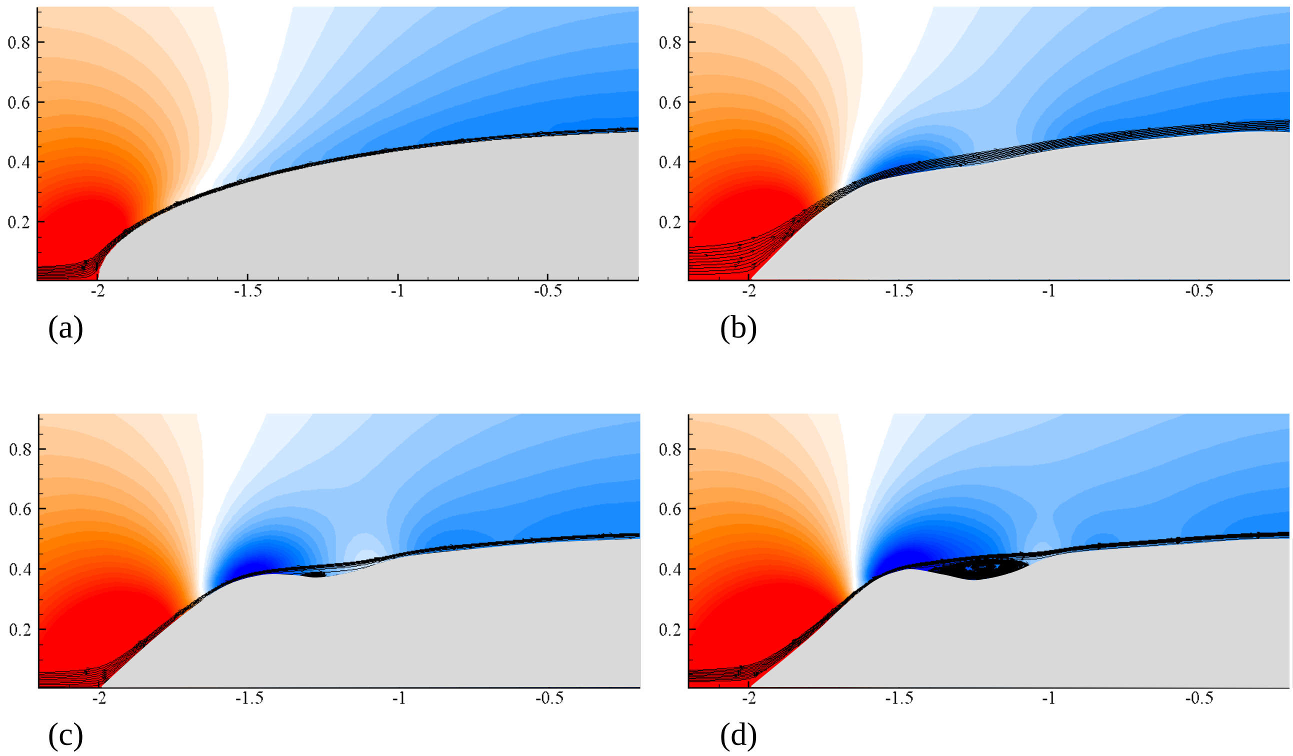

Figure 3.2. Time-averaged streamline and pressure contours at $Re = 10^3$: (a) 4:1 ellipsoid; (b) Case1; (c) Case2; (d) Case3.

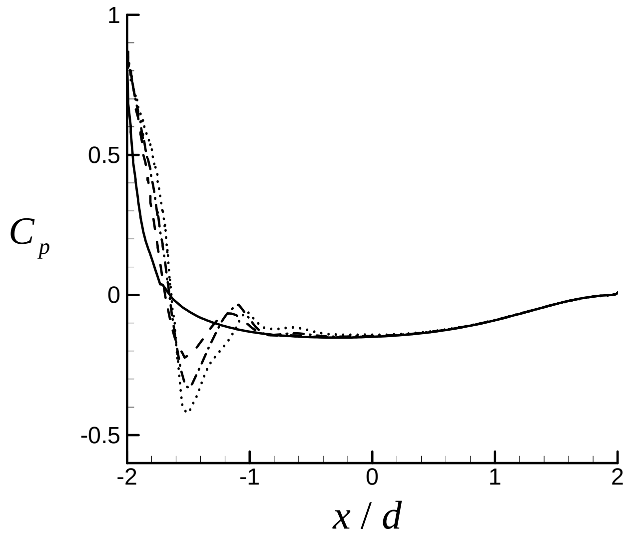

(a)

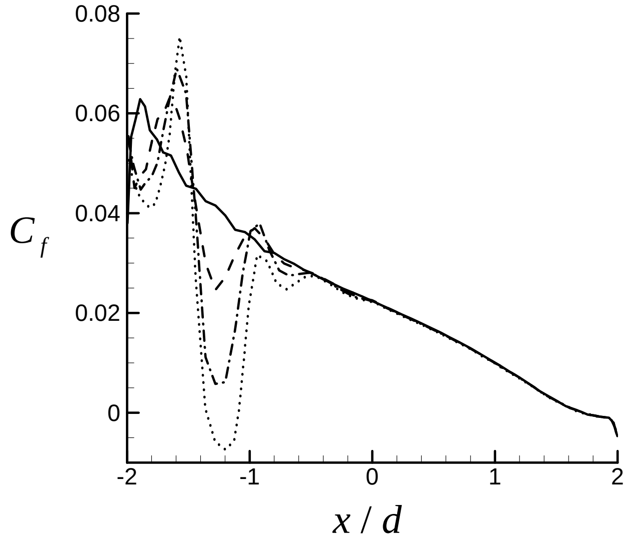

(b)

Figure 3.3. Flow variables along the body surface at $Re = 10^3$: (a) pressure drag coefficient (b) friction drag coefficient. —, 4:1 ellipsoid; - - -, Case1; $- \cdot -$, Case2; $\cdots$ Case3.

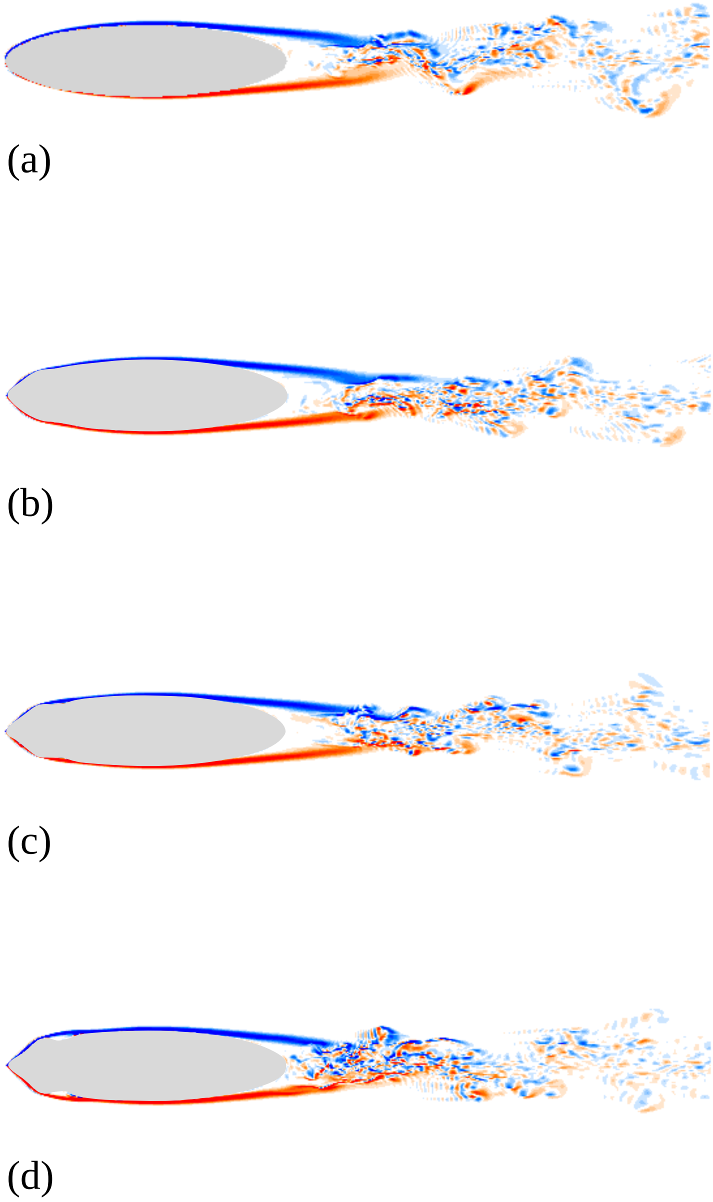

Figure 3.4. Contours of the instantaneous azimuthal vorticity in x-y plane at $Re = 10^4$: (a) 4:1 ellipsoid; (b) Case1; (c) Case2; (d) Case3.

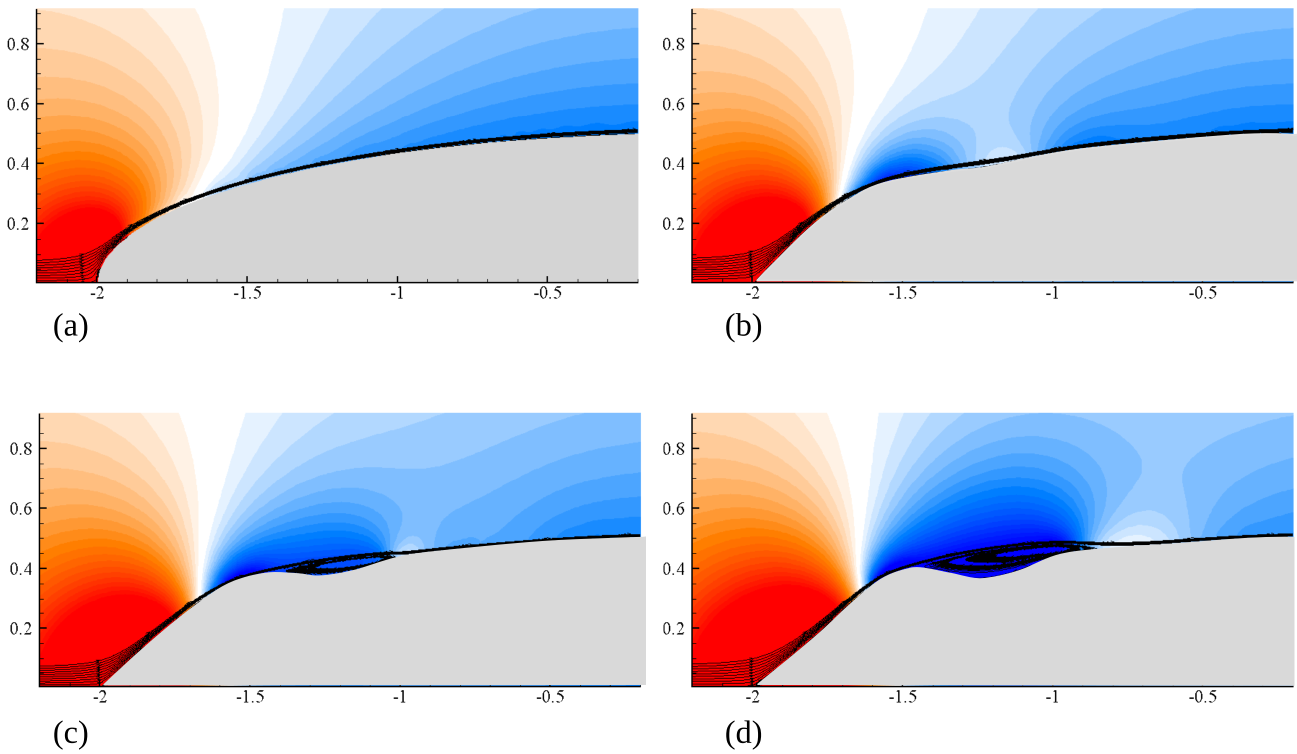

Figure 3.5. Time-averaged streamline and pressure contours at $Re = 10^4$: (a) 4:1 ellipsoid; (b) Case1; (c) Case2; (d) Case3.

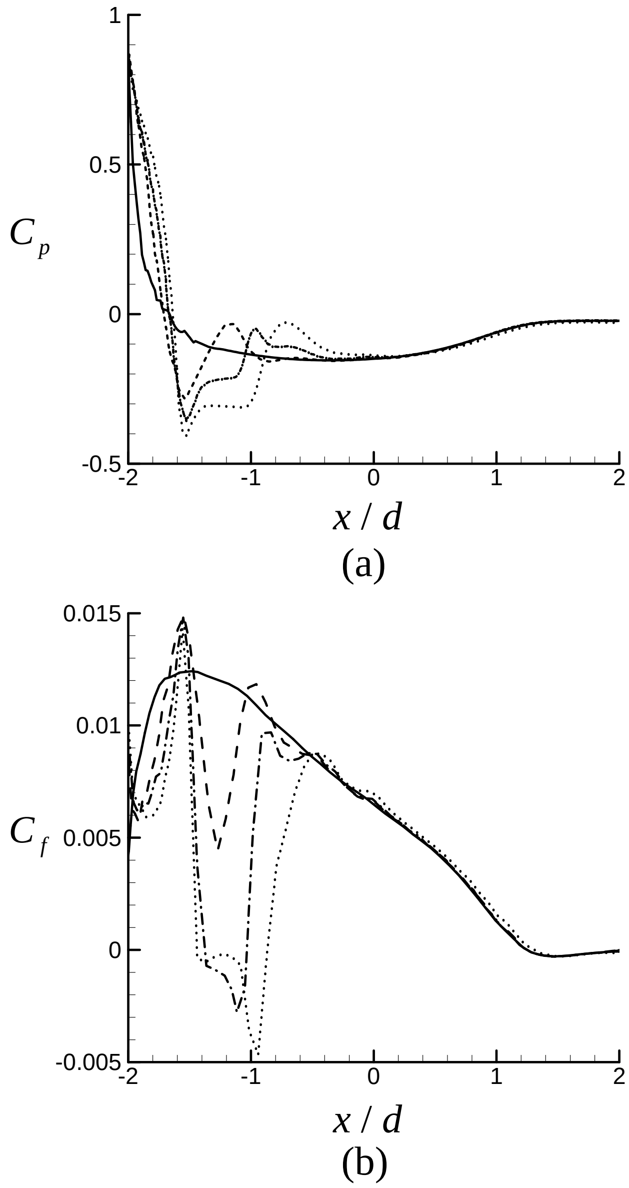

Figure 3.6. Flow variables along the body surface at $Re = 10^4$: (a) pressure drag coefficient (b) friction drag coefficient. —, 4:1 ellipsoid; - - -, Case1; $- \cdot -$, Case2; $\cdots$ Case3.

Chapter 4

Summary and Conclusions

In the present study, we investigated the effect of forebody curvature of an axi-symmetric body by numerical simulation. Curvatures were applied to forebody of 4:1 ellipsoid, maintaining volume of body. Flow around body in laminar flow at Reynolds number 10^3 and turbulent flow at 10^4 were considered.

At $Re = 10^3$, we found little difference on drag of body with forebody curvature compared to 4:1 ellipsoid. As curvature increased, pressure drag increased due to low pressure around the forebody curvature. On the other hand, friction drag decreased as curvature increased due to the formation of recirculation bubble on concave region of curvature. The amount of increase in pressure drag and decrease in friction drag are similar.

At $Re = 10^4$, total drag changed depending on forebody curvature. Total drag decreased as curvature increased in certain range, but it increased when curvature became too large. The maximum drag reduction is about 4.5%. Pressure drag and friction drag showed similar trend to laminar flow at $Re = 10^3$. As curvature increased, pressure drag increased but friction drag decreased. Recirculation bubble on the curvature expanded over concave region and it had much larger size compared to that of laminar flow, resulted in total drag variation.

References

Akselvoll, K. & Moin, P. 1996 An efficient method for temporal integration of the Navier-Stokes equations in confined axisymmetric geometries. *J. Comput. Phys.* **125**, 454–463.

Bannasch, R. 1998 Hydrodynamcis of wave-like curvature on bodies of swimming animals. *Proceedings of the Ninth Inernational Offshore and Polar Engineering Conference*

Clark, BD & Bemis, W. 1979 Kinematics of swimming of penguins at the Detroit Zoo. *J. Zool., Lond* **188**, 411–428.

Kim, J., Kim, D. & Choi, H. 2001 An immersed-boundary finite volume method for simulations of flow in complex geometries. *J. Comput. Phys.* **171**, 132–150.

Lee, J., Choi, H. & Park, N. 2010 Dynamic global model for large eddy simulation of transient flow. *Phys. Fluids* **22**, 075106.

Park, N., Lee, S., Lee, J. & Choi, H. 2006 A dynamic subgrid-scale eddy viscosity model with a global model coefficient. *Phys. Fluids* **18**, 125109.

Yun, G., Kim, D. & Choi, H. 2006 Vortical structures behind a sphere at subcritical Reynolds numbers. *Phys. Fluids* **18**, 015102.

전두부 곡률 형상이 항력에 미치는 영향

서울대학교 대학원
기계항공공학부
장윤식

요약

본 연구에서는 전두부 곡률 형상이 축대칭 물체의 항력에 미치는 영향을 수치적으로 분석하였다. 곡률 형상은 종횡비가 4:1 인 타원체에 적용되었으며 물체의 단축과 자유유동속도를 기준으로 한 레이놀즈 수 10^3 과 10^4 에서 계산을 수행하였다.

레이놀즈 수 10^4 에서는 4.5%의 총 항력 감소를 얻었다. 하지만 레이놀즈 수 10^3 에서는 총 항력의 변화가 거의 없었다. 두 레이놀즈 수 모두에서 곡률이 증가할수록 전두부 곡률 주변에서 낮은 압력이 형성되어 압력 저항이 증가한다. 마찰 저항은 곡률의 오목한 부분에 생성되는 재순환 보텍스에 의하여 곡률이 증가할수록 감소한다. 따라서 총 항력의 감소는 전두부 곡률 형상에 따른 압력 저항의 증가량과 마찰 저항의 감소량의 크기에 의해 결정된다.

주요어: 전두부, 곡률, 항력, 타원체

학번: 2010-24071